Materials and Design 183 (2019) 108169

Contents lists available at ScienceDirect

Materials and Design

journal homepage: www.elsevier.com/locate/matdes

Unraveling indentation-induced slip steps in austenitic stainless steel

Wenzhen Xia *, Gerhard Dehm , Steffen Brinckmann *

Department of Structure and Nano-/Micromechanics of Materials, Max-Planck-Institut für Eisenforschung GmbH, Max-Planck-Straße 1, 40237, Düsseldorf, Germany

HIGHLIGHTS

- Slip steps occurring on positively and negatively inclined slip planes are found during indentation.
- Slip steps on negatively inclined slip planes form due to the change in surface topography.
- Three discriminant methods about identification of slip step are proposed.
- Origin and occurrence sequence of slip on positively and negatively inclined planes are revealed.

GRAPHICAL ABSTRACT

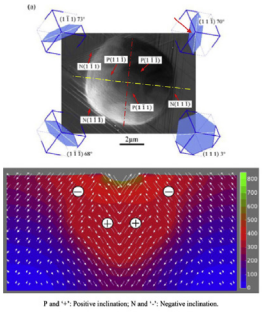

P and '+': Positive inclination; N and '-': Negative inclination.

ARTICLE INFO

Article history:
Received 7 May 2019
Received in revised form
27 August 2019
Accepted 29 August 2019
Available online 3 September 2019

Keywords:
Nanoindentation
Slip step
Plasticity
Austenitic stainless steel

ABSTRACT

Nanoindentation has been used intensively during the last decades to characterize experimentally the elastic and plastic material properties of phases at the microscale. Accompanying simulations have investigated the plastic mechanisms during nanoindentation. While experiments and simulations have led to a thorough understanding of most mechanisms during nanoindentation, the plasticity on positively and negatively inclined slip planes is still not completely clear. In this work, {1 0 0}-, {1 0 1}- and {1 1 1}-grains of an austenitic stainless steel are indented to better understand the dislocation mediated plasticity through slip step analysis. We observe that slip occurs on positively and negatively inclined slip planes during nanoindentation and we propose methods to differentiate between both types of planes. We find that slip steps on positively inclined slip planes form preferentially during the early stage as compared to the formation of slip steps on negative inclination, which occurs during the later deformation stage due to the change in surface topography. By calculating the resolved shear stress in the presence and absence of pile-ups, we reveal the origin of slip on positively and negatively inclined planes as well as the reason for the sequence of occurrences. We conclude that accounting for the surface topography evolution in experiments and simulations is essential in predicting the plastic slip activation during nanoindentation.

1. Introduction

Metal plasticity is associated with dislocation motion on specific crystallographic planes. In polycrystalline metals, the grain orientation and the stress on the individual grain determine the plastic microscale deformation, which is controlled by the activated slip systems and by the resolved shear stress, i.e. Schmid's law [1,2]. Nanoindentation has been used to unravel the plastic deformation mechanisms and mechanical properties of metals at small scales [3–16]. The corresponding load versus penetration depth data (often called the P-h curve) provides rich information, e.g. hardness and elastic modulus [4–7]. Based on geometrically necessary dislocations (GND) under the indenter, Nix and Gao [8] proposed a

* Corresponding author.
E-mail addresses: w.xia@mpie.de (W. Xia), brinckmann@mpie.de (S. Brinckmann).

https://doi.org/10.1016/j.matdes.2019.108169

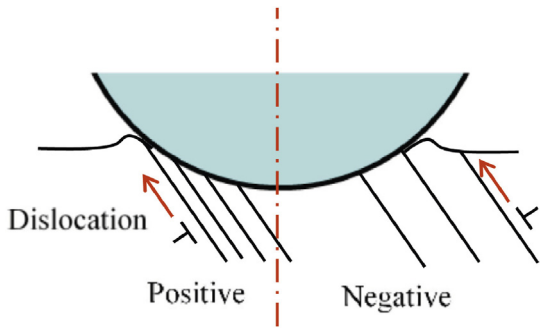

Fig. 1. Schematic diagram of positively and negatively inclined slip planes.

model to describe the indentation size effect (ISE), i.e. shallow indention results in increased hardening compared to deeper indentation. Moreover, during nanoindentation the indenter spontaneously moves into metals without an increase in the applied load. This displacement-burst is called 'pop-in' [3] and is connected to the dislocation nucleation and multiplication [17,18]. Tromas et al. [19,20] stopped the nanoindentation in MgO after the pop-in to study the incipient plasticity. They reconstructed the dislocation structures by nanoetching and atomic force microscopy (AFM). Their results revealed that the dislocations are nucleated at the point of maximum resolved shear stress underneath the indenter and that the dislocations move upward to the surface. Velednitskaya et al. [21] determined the dislocation structure and the Burgers vectors of the dislocations around the MgO indentation through transmission electron microscopy (TEM) and scanning electron microscopy (SEM). They mentioned that the dislocations, which originate from underneath the indenter, do not explain fully the pile-up that surrounds the indentation.

Nibur, et al. [22,23] identified slip steps around residual imprints into a face-centered cubic (FCC) metal using Electron Backscatter Diffraction (EBSD) and AFM. They proposed to divide slip planes into 'positively inclined slip planes' and 'negatively inclined slip planes', as shown in Fig. 1. The dislocations move on the positively inclined slip planes from underneath the indenter, i.e. from the area of highest shear stresses, to the surface. The dislocations move on the negatively inclined slip planes from the outside perimeter to the surface and closer to the imprint. The authors found that 'stair-like' slip steps form due to positively inclined slip planes and that the 'serrated' shape is formed by negatively inclined slip planes. The causes of grain orientation and indentation tip geometry on slip step evolution were also analyzed by calculating the resolved shear stress. However, the authors did not fully address the occurrence of slip on negatively inclined planes and the sequence of slip events.

Dislocation mediated plasticity during indentation was studied by a number of authors using methods ranging from mesoscale crystal plasticity based finite-element simulations (CP-FEM), via microscale dislocation dynamics simulations (DD) to nanoscale molecular dynamics (MD). Using CP-FEM, Eidel [24] analyzed the indentation pile-up pattern in a FCC Ni-superalloy and reported that dislocations glide on {1 1 1}⟨1 1 0⟩ slip systems from underneath the indenter tip to the surface, i.e. positively inclined slip planes, and that this deformation results in the pile-up formation. Wang et al. [25] studied in FCC copper single crystals the effects of crystallographic orientations on the pile-up patterns during nanoindentation with a *conical* tip through 3D elastic-viscoplastic CP-FEM: the pile-up patterns on the {0 0 1}-, {0 1 1}- and {1 1 1}-surfaces exhibit a four-, two-, six-fold symmetry, respectively. Wang et al. [26] performed experiments and 3D CP-FEM simulations for indentation with a *Berkovich* tip into copper single crystals. They found that the indenter geometry induces the specific stress distribution that strongly affects the pile-up topography and which modifies the pile-up symmetry on the {0 0 1}-, {0 1 1}- and {1 1 1} surfaces.

Using DD, Han et al. [27] determined a surface induced size effect during nanoindentation. They found that a free surface acts either as a dislocation sink or dislocation source depending on the surface proximity of the dislocation source. Widjaja et al. [28] used 2D dislocation dynamics to observe mostly dislocation activity on positively inclined planes and prismatic dislocation activity. Fivel et al. [29,30] used 3D dislocation dynamics to analyze the plastic zone during indentation. It was observed that the dislocations form prismatic loops that move from the indenter into the material and that these prismatic dislocation loops are geometrically necessary dislocations. As such, these prismatic dislocations move on planes that are neither positively nor negatively inclined. Gagel and Weygand [31] also observed prismatic dislocation loops that are similar to those of Fivel et al. and that were compared to experiments on a {1 1 1} copper surface [32,33]. However, those previous CP-FEM and DD simulations neglected the large deformation and the pile-up formation, which potentially change the activated slip planes.

Using MD, Lodes et al. [17] investigated the pop-in mechanisms and the dislocation activity underneath indenters. Begau et al. [34,35] observed prismatic dislocation loops in a Cu single crystal during nanoindentation and identified the mechanisms that result in the formation of prismatic loops. Stukowski and Arsenlis [36], Jiao et al. [37], Alhafez et al. [38] simulated the indentations into a {1 1 1}- surface of a Cu thin film, (1 0 0) surface of Al and a CoCrFeMnNi FCC high-entropy alloy, respectively. They also found prismatic dislocation loops nucleating beneath the indenter and moving into the material. Varillas et al. [39] studied nanoindentation for Cu and showed that the slip traces along the ⟨0 1 1⟩ and ⟨1 1 2⟩ directions are caused by dislocation interaction. The slip traces on the (1 1 1) surface had a triangular shape and form on positively inclined {1 1 1} slip planes.

Even though many experiments and simulations have studied indentation induced plasticity, a thorough understanding is still unclear. Dislocation activity has been observed experimentally and numerically on planes, which Nibur and Bahr defined as positively inclined planes. In addition, dislocation and molecular dynamics predict prismatic dislocation loops that have been also observed experimentally in high speed indentation [31,32]. Although Nibur and Bahr [22,23] also observed dislocation slip on negatively inclined slip planes, those authors did not address the mechanisms that resulted in this slip and the reason for the change in slip plane activity. In this work, we address the mechanisms that lead to slip on negatively inclined slip planes and the sequence of slip events.

The main objective of this work is to improve the understanding of dislocation activity on positively and negatively inclined slip planes. Towards this goal, we study the plasticity during nanoindentation in austenitic steel and find the change of slip activation from positively to negatively inclined slip planes. We use differentiation methods that allow discriminating between both slip plane inclinations. These experimental methods include EBSD, AFM and Electron Channeling Contrast Imaging (ECCI). We perform FEM simulations to calculate the change of the stress state that leads to a change in resolved shear stress and the activation and deactivation of slip planes. We emphasize that accounting for the surface topography evolution, i.e. evolution of the pile-up, is essential for understanding plasticity during indentation.

2. Experimental procedure

The as-received austenitic stainless steel Fe-25Cr-20Ni (FCC) with a stacking fault energy (SFE) around 45 mJ/m^2 [40] was

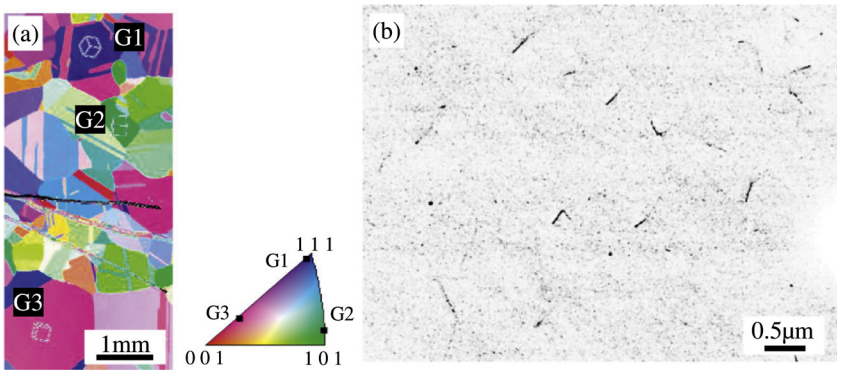

Fig. 2. (a) Inverse pole figure (IPF) determined by EBSD before indentation with the three selected grains. G1 is close to {1 1 1}, G2 is close to {10 1} and G3 is close to {0 0 1} orientation. (b) ECCI image of the defect state in grain {1 0 1} before testing (inverted grayscale; dark lines are dislocations).

annealed at 1200 °C for 168 h and then water quenched to room temperature to obtain a coarse grained microstructure with an average grain size of 650 μm. As these grains were significantly larger than the indenter contact area, the nanoindentation measurements were only determined by the individual grain response while reducing the influence of grain boundaries or secondary phases (at the grain boundaries). The sample was ground, followed by mechanical polishing that included a 50 nm colloidal silica suspension. The sample was etched with a V_2A solution (10 ml HNO_3, 0.30 ml Vogels pickling inhibitor, 100 ml HCL and 100 ml H_2O) for 30 s to remove the deformation layer that developed by the intermediate preparation. As final step, the sample was polished for 30 min by colloidal silica to remove the chemically produced layer [41]. EBSD in a JEOL 6490 SEM was used to identify grains whose orientations are close to the {1 1 1}, {1 0 1} and {0 0 1} direction, as shown in Fig. 2(a). The initial defect state was quantified by ECCI in a Zeiss-Merlin: the initial dislocation density is about 1×10^{12} m^{-2}, as shown in Fig. 2(b).

For indentation, we used a Keysight/KLA G200 nanoindenter with an $r = 10$ μm spherical diamond tip and 0.5 mN/s loading and unloading rate. Normal forces of 2, 5, 10, 20, 40 and 80 mN were employed to create different indentation depths in the three grains. The indents were sufficiently spaced (35 μm) to avoid mutual interaction of the indentations. The indents were inspected in a SEM with a secondary electron (SE) and a backscatter electron detector (BSD). The SE images were captured with an acceleration voltage of 3 kV and a probe current of 6000 nA. A voltage of 30 kV and a current of 2000 nA were used to obtain the ECCI images. In addition, the surface topographies were measured by AFM (Veeco Digital Instruments, Plainview, New York, DI3100S-1).

In this study, we identify slip steps on the surface by SEM and use three methods (1) to correlate the slip steps to specific planes and (2) to differentiate between positively inclined and negatively inclined slip:

- EBSD: This method only determines the crystal orientation to correlate slip steps and slip planes. This method is the simplest but it is in many cases ambiguous since the alignment of EBSD is limited and since slip steps might be correlated to either of two planes.
- EBSD and ECCI: This method identifies the crystal orientation by EBSD and uses ECCI to visualize near-surface dislocation lines. These dislocation lines help to distinguish between slip on different slip planes. ECCI visualizes dislocations on specific planes while other dislocations on other planes are invisible for certain two-beam imaging conditions (i.e. sample tilt) [41].
- EBSD and AFM: ECCI is an advanced method which emphasizes dislocations on certain planes; some slip planes cannot be inspected due to stage tilting limitations. Therefore, the combination of EBSD and AFM allows to identify the crystal orientation and AFM is used to differentiate between the slip step patterns. This method is based on the work of Nibur and Bahr [22,23].

We use and discuss the applicability of the three methods to differentiate between slip on positively inclined and negatively inclined planes.

3. Experimental results

Fig. 3 shows the SE image of the 80 mN indentation into the {1 1 1} grain. The four {1 1 1} slip planes in the crystal unit cell are highlighted in the corners. The slip steps are visible on the $(1\bar{1}1)$, $(11\bar{1})$, and $(1\bar{1}\bar{1})$ slip planes, while no slip activity occurred on the (1 1 1) plane. The three active slip planes are inclined at an angle of ~70° to the surface. On the other hand, the (1 1 1) slip plane has an angle of 3° and the resolved shear stress is neglectable. The resulting slip step pattern has the shape of two sets of equilateral triangles that are nested inside each other, with the pattern center coinciding with the center of indentation.

As for all grain orientations, parallel slip planes are separated by the indentation centerline into positively inclined and negatively inclined slip planes [23]: e.g. a $(11\bar{1})$ plane has a positive inclination on the left side of the yellow centerline in Fig. 3(a), and a $(11\bar{1})$ plane has a negative inclination on the right side of the centerline. It should be noted that there is a unique centerline to each group of parallel slip steps, i.e. the intersection line of the slip plane with the surface, see Fig. 3(b). Hence, the slip step pattern on the {1 1 1} grain shows dislocation activity on the positive and negative slip planes of the three active slip plane groups.

Fig. 4 shows the topographies of 2, 5, 10 mN imprints into the {1 1 1} grain. After indentation with 2 mN, slip steps on positively inclined planes form an equilateral triangle on the surface. After indentation with 5 mN, the hexagonal slip pattern around the imprint is visible, which was produced by slip on positively and negatively inclined planes. Moreover, the steps on the positively inclined slip planes fill up the whole inside of the imprint and all slip steps on negatively inclined planes form at the imprint outside. As shown in Fig. 4(c), slip steps on negatively inclined slip planes become more abundant after indentation with 10 mN and these slip steps especially occur at the ends of previously created slip steps on positively inclined planes.

In the corresponding ECCI image, Fig. 4(d), we observe an array of bright spots on the positively inclined $(1\bar{1}\bar{1})$ plane after indentation with 2 mN. This array of bright spots suggests that the dislocations are conventional dislocation loops, rather than the prismatic loops. Fig. 4(e) shows the load-depth curves of the nanoindentation measurements with different normal forces. All curves have the same loading curve and the same elastic unloading

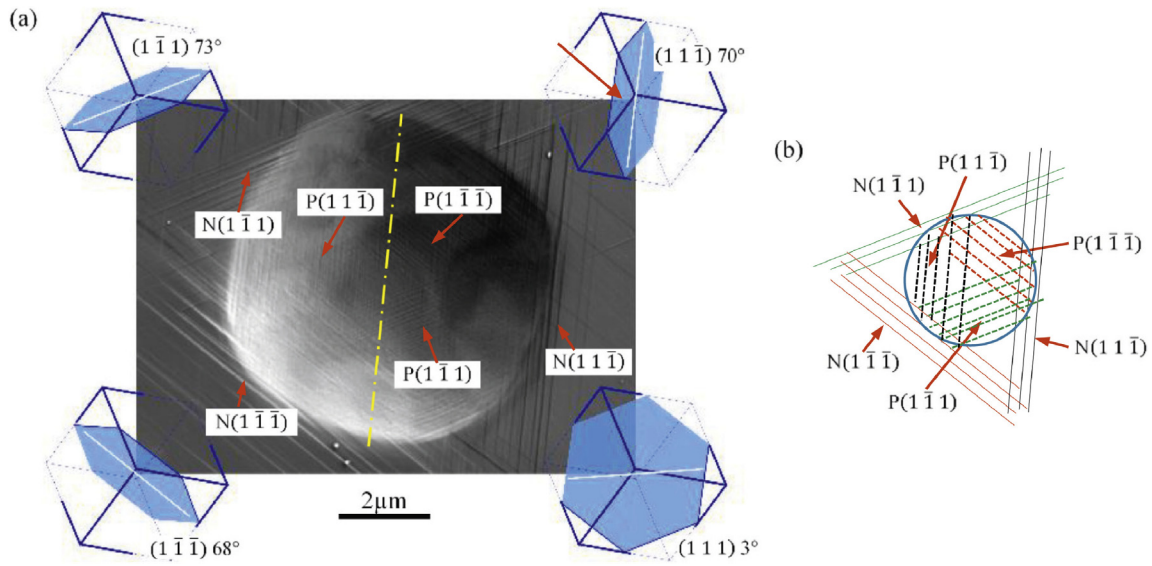

Fig. 3. (a) SE image and (b) schematic diagram of the 80 mN indentation into the {1 1 1} grain with P for 'positively' and N for 'negatively inclined slip plane'.

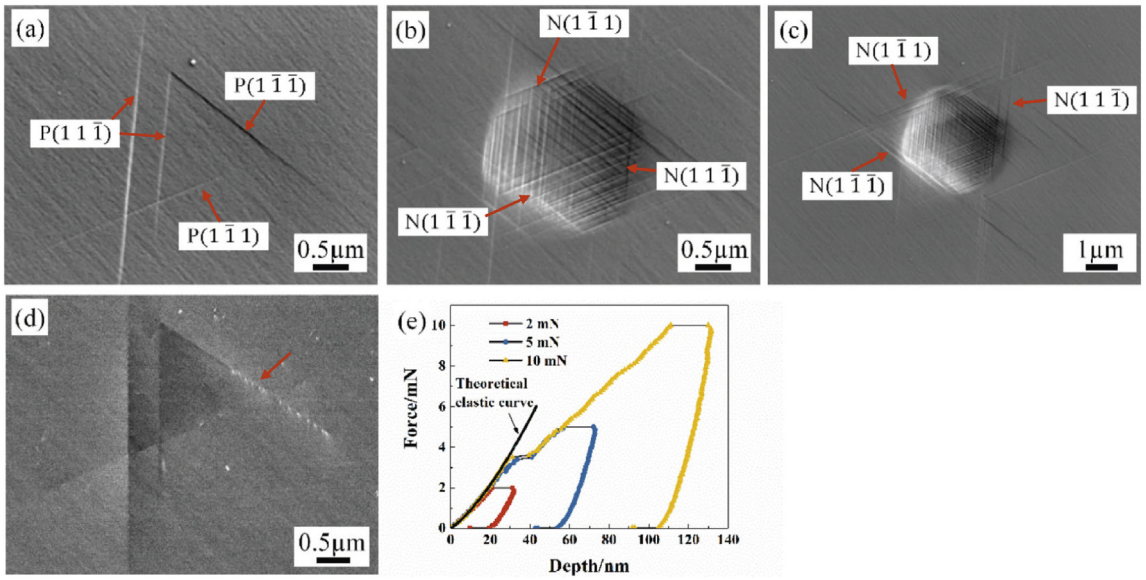

Fig. 4. Topographies of the indentation with (a) 2 mN, (b) 5 mN and (c) 10 mN in the {1 1 1} grain. Please note the different scales in (c) to show the entire indentation imprint. (d) ECCI image of the dislocation distribution in (a). (e) the corresponding load-displacement curves with the theoretical curve according to the Hertz solution.

slope. The pop-in for the indentation with 2 mN is at 2 mN, which relates to a maximum shear stress of 1.3 GPa. During the pop-in, dislocations were nucleated underneath the indenter and their slip steps are present on the surface after the experiment. Hence, these pop-in dislocations traveled on positively inclined slip planes. The curves for the indentation with 5 mN and 10 mN show a pop-in at 3.5 mN, which relates to a maximum shear stress of 1.5 GPa underneath the indenter. Both curves have a significant increase in depth at the load maximum, although no hold time is used in these experiments. The depth increase occurs during the short time that is required for indenter motion reversal. The elevated pop-in load and the depth increase during indenter motion reversal are the result of the fast indenter motion, which does not result in a stationary dislocation structure.

Fig. 5 shows the SE and ECCI images after 80 mN indentation into the {1 0 1} grain; specifically a $(01\bar{1})$ oriented grain. The angles of 4 slip planes with respect to the surface are shown in Fig. 5(a). Slip steps are observed on positively inclined and negatively inclined planes of all four slip plane groups. As the slip steps of the $(1\bar{1}1)$ and $(11\bar{1})$ planes are almost parallel, ECCI is used to differentiate between the two planes. We inspect by ECCI region 'A' (see Fig. 5(a) and (b)) and sketch the location of the imprint, the slip step lines and the observed dislocations in Fig. 5(c). An array of dislocation lines is marked with red arrows: these dislocations are on the right-hand side of slip step lines and hence move on the $(11\bar{1})$ slip plane, which is in this location negatively inclined. The dislocation lines marked by a yellow arrow are located on the left-hand side of slip step and these dislocations move on positively inclined $(1\bar{1}1)$ slip planes.

Fig. 6 shows the SE images of indentation with 2 mN and 5 mN into the {1 0 1} grain. After indentation with 2 mN, the slip steps develop on positively inclined $(11\bar{1})$ and $(1\bar{1}1)$ slip planes. By contrast, the slip steps on (1 1 1) and $(1\bar{1}\bar{1})$ planes, that are almost perpendicular to surface, are distributed on both two sides of corresponding centerline. After indentation with 5 mN, we observed

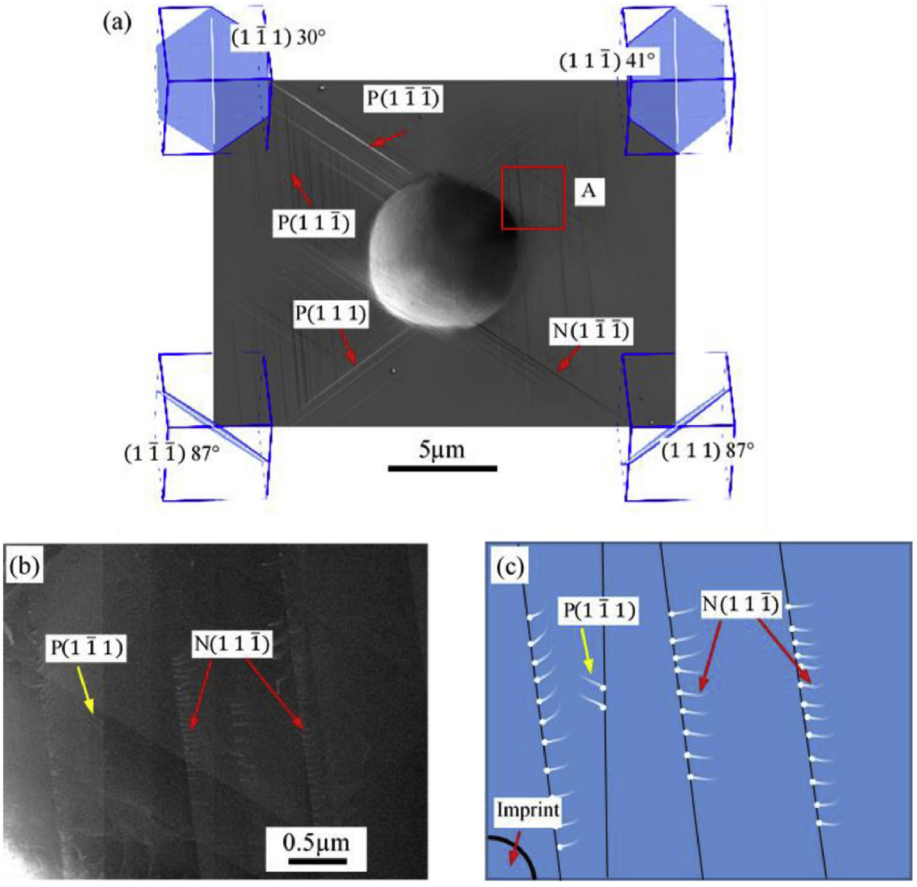

Fig. 5. (a) SE and (b) ECCI images of the 80 mN indentation into the {1 0 1} grain and (c) schematic diagram of the imprint, the slip lines and the dislocation distribution in the ECCI image.

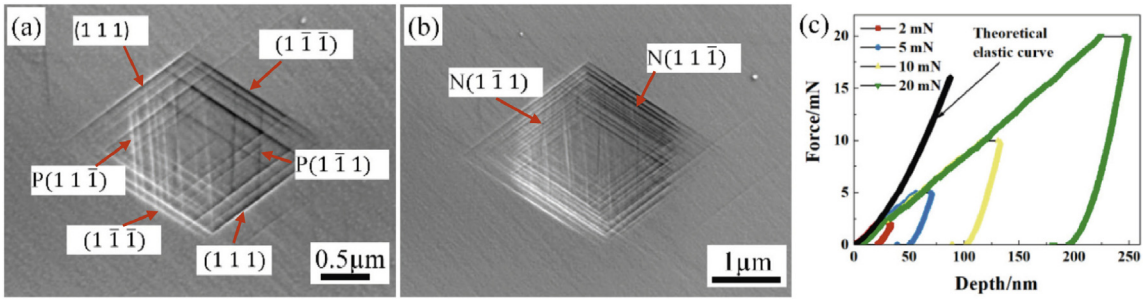

Fig. 6. SE images of the indentation with maximum loads of (a) 2 mN and (b) 5 mN in the {1 0 1} grain. (c) The force-depth curves of the corresponding indentation experiments. SEM images of 10 mN and 20 mN are not shown here for conciseness.

slip steps on negatively inclined $(11\bar{1})$ and $(1\bar{1}1)$ planes. However, the slip step density on the (1 1 1) and $(1\bar{1}\bar{1})$ planes is significantly higher than on the other two slip planes.

The corresponding force-depth curve of the indentation with 5 mN does not reveal a distinct pop-in but the curve transitions continuously from the theoretical elastic curve according to the Hertz solution to the plastic curve. The curves for the 2 mN and 5 mN indentations have an extended depth increase at the maximum force as a result of the high loading rate. The extended plasticity in both force-depth curves relates to the large imprint and the slip steps in the SEM images.

The corresponding ECCI figures are shown in Fig. 7. The bright spot array on the (1 1 1) and $(1\bar{1}\bar{1})$ slip planes after indentation with 2 mN (a) and 5 mN (b) are marked by red arrows. It reveals that the dislocations are not prismatic loops. Fig. 7(a) confirms that the slip step lines (marked by the red circle) formed on positively inclined slip planes.

The initial dislocation density is 1×10^{12} m^{-2} in the {101} grain, as shown in Fig. 2(b). This initial dislocation density is low compared to ~10^{13} m^{-2} for Fe-25Cr-20Ni steel after annealing [42], because the sample for this study is heat treated for a long time to reduce the dislocation density. As shown in Fig. 7(a), after indentation the dislocation density is about 7×10^{12} m^{-2} in the perimeter of the imprint, i.e. distant from the axis of indentation. This value is increased compared to the initial state. However, it should be noted that the numerous dislocations are activated underneath and close to the imprint. These dislocations are invisible and hence, the given dislocation density is a distant lower boundary for the expected dislocation density after nanoindentation.

After indentation with 5 mN, a few dislocations on negatively inclined $(11\bar{1})$ planes are found, see yellow circle in Fig. 7(b) and (c). As the deformation increases, the dislocations multiply and travel

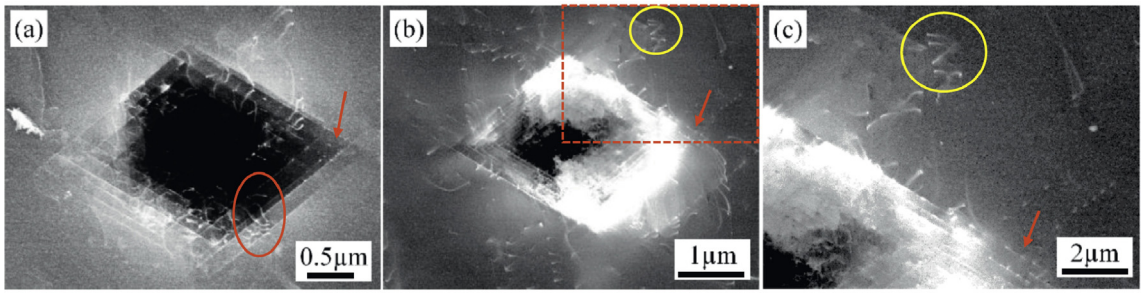

Fig. 7. ECCI images of the indentation with maximum loads of (a) 2 mN, (b) and (c) 5 mN in the {1 0 1} grain. (c) is the zoom of the area marked by a red dashed frame in (b). (For interpretation of the references to color in this figure legend, the reader is referred to the web version of this article.)

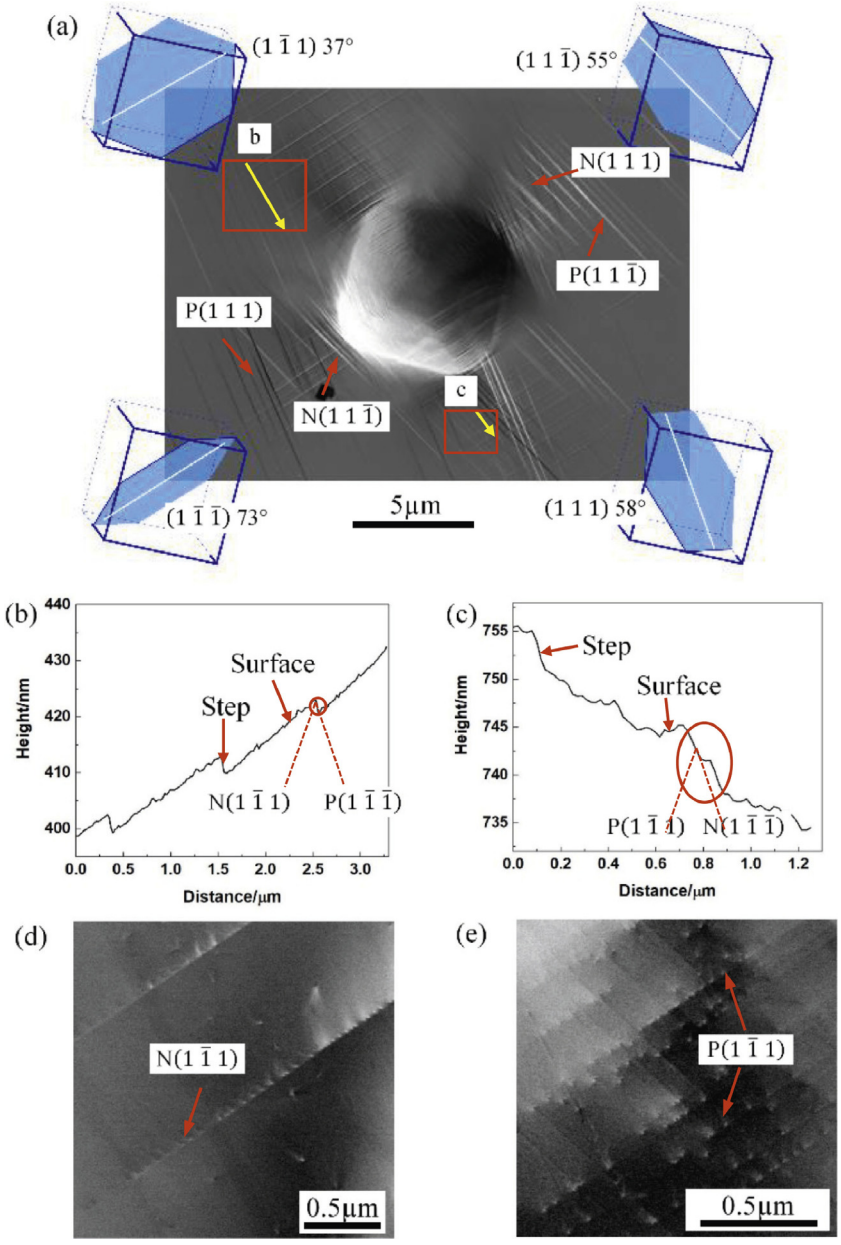

Fig. 8. (a) SE image of the 80 mN indentation into the {0 0 1} grain. (b) and (c) AFM height profiles along the yellow lines 'b' and 'c'. (d) and (e) ECCI images on the red marked areas b and c. (For interpretation of the references to color in this figure legend, the reader is referred to the web version of this article.)

away from the contact area on the active slip planes.

The 80 mN indentation into the {0 0 1} grain is shown in Fig. 8. The slip steps that develop due to plasticity on the $(11\bar{1})$ and (1 1 1) slip planes are identified by the SEM (see Fig. 8(a)). The slip steps originating from the $(1\bar{1}1)$ and $(1\bar{1}\bar{1})$ planes are almost parallel and more difficult to distinguish. Here, we use AFM of the top-left and bottom-right domains to determine the topography and to distinguish between activity on slip planes that have almost parallel steps. The height profiles along the yellow arrows 'b' and 'c' are presented in Fig. 8(b) and (c), respectively. The topography steps on the top-left domain 'b' have a serrated morphology while the topography steps have stair-shape on bottom-right 'c', see also Nibur et al. [23]. In the present study, ECCI observations reveal that these slip lines arise from negatively inclined $(1\bar{1}1)$ planes on the top-left area 'b' and from positively inclined $(1\bar{1}1)$ planes on the bottom-right area 'c', as shown in Fig. 8(d) and (e). Hence, slip on positively inclined planes results in stair-shaped topologies while slip on negatively inclined planes results in a serrated topology.

4. Discussion

4.1. General discussion and identification of slip plane inclination

The goal of this study is to (1) understand the grain orientation dependent characteristic slip step patterns that are created during indentation and (2) identify whether the activated slip planes are positively or negatively inclined. Before the results of the current study are discussed, we investigate how the general nanoindentation characteristics might affect the transferability of the present results.

Nanoindentation leads to an indentation size effect due to the strain gradients and geometrically necessary dislocations. This small-scale behavior is consistently described by the Nix-Gao model [8] and this behavior also occurs in this study but that mechanism does not address the observed inversion of slip-plane activity: i.e. the indentation size effect explains a decrease/increase of strain gradients; but the indentation size effect does not explain a change of the stress state.

At the nanoscale, experiments in the transition from elastic to plastic deformation have a statistical variance that is much larger than at the macroscale. This variance is due to the sampling of volumes that may have zero, one or more dislocations in them. As a result, these volumes have severely different mechanical responses due to the initial dislocation density. It should be emphasized that each different volume deformation is the *true* (but local) material response to the different initial condition. The present experiments also depend on the statistical initial condition, which leads to *different slip-step patterns*, e.g. in one experiment of the {111} grain, the slip on $(1\bar{1}1)$ is larger than the slip on $(\bar{1}11)$; in another experiment, the comparison between $(1\bar{1}1)$ and $(\bar{1}11)$ might change. This statistical initial dislocation configuration also leads to different transitions from the elastic to the plastic domain, i.e. pop-in. If − by chance − we stop indentation precisely during the pop-in, then we observe the initial deformation, e.g. Fig. 4(a). However, the statistical variation is minimal in the purely elastic regime and after accumulation of large amounts of plasticity. Hence, (1) the elastic curves before the pop-in, (2) the elastic unloading curves as well as (3) the plastic indentation curves are repeatable in the experiments of this study, see Fig. 4(e).

Towards the goal of this study, we investigate the deformation of {1 1 1}, {1 0 1} and {0 0 1} grains and use combinations of different tools to distinguish between the slip plane inclinations: (1) EBSD, (2) EBSD + ECCI, (3) EBSD + AFM. The slip steps on the {1 1 1} grain and the slip plane inclination are determined by EBSD since the angles between the slip step lines are sufficiently large, as shown in Fig. 3(a). We differentiate between positively and negatively inclined slip planes by using the crystal orientation as identified by EBSD, the corresponding centerlines of the slip steps and the location of the actual slip steps. This differentiation method sufficiently distinguishes between positively and negatively inclined slip planes Fig. 3(b) for the {1 1 1} grain.

When the slip step lines from different planes are almost parallel, e.g. on the {1 0 1} grain, ECCI together with EBSD can be used to differentiation into positively and negatively inclined planes. This differentiation method is required because the angle between the slip step lines is not larger than the EBSD tolerance angle (see Fig. 5(a)). Once conventional dislocation loops move towards the surface, these closed dislocation loops are opened and the two loop ends are visible by ECCI: the ends are bright surface dots with fading dislocation line intensities into the depth. Such information is used to unambiguously determine the slip plane inclination. If the fading dislocation lines are located on the imprint side of slip step, the dislocations travel on a positively inclined slip plane away from underneath the indentation. If the fading lines are on the opposite side, then the planes are negatively inclined as they form a roof-shape.

To differentiate the slip plane tilting, the combination of EBSD and AFM is useful in some cases when the slip steps on the pile-ups are almost parallel to the imprint perimeter; see Fig. 8(a). Since slip steps originate from dislocation motion, the material in the serrated areas (marked with red circle in Fig. 8(b)) has to be attributed to the $(1\bar{1}1)$ slip plane, rather than the $(1\bar{1}\bar{1})$ plane that would intersect the surface topography. In Fig. 8(c), the stair-case slip steps are parallel to the $(1\bar{1}1)$ plane but not parallel to the $(1\bar{1}\bar{1})$. As such, the shape of the slip steps differentiates slip on positively (serrated topology) and negatively inclined planes (stair-case topology) [23]. Please note that we used ECCI inspection to confirm this AFM-based differentiation, as shown in Fig. 8(d) and (e).

The aforementioned differentiation between positively and negatively inclined slip planes is based on conventional dislocation loops, rather than prismatic loops that were observed in FCC metals under some circumstances. Miura et al. [32,43] experimentally observed prismatic dislocation half loops on the {1 1 1} copper surface after high velocity indentation by a falling sphere. Gagel et al. [31] revealed the formation mechanisms of prismatic half loops using 3D DD, which employs a fast loading rate. Chang et al. [44] reproduced full prismatic loops by DD simulations with a high deformation rate. Voyiadjis et al. [45] and Stukowski et al. [36] use large-scale MD simulations with a very fast loading rate to reveal the formation of full prismatic loops during indentation into the {1 1 1} surface. In our nanoindentation experiments with a moderate deformation rate compared to MD simulations, however, the arrays of bright dislocation dots in ECCI images reveal that these dislocations are not prismatic loops, as shown in Fig. 4(d).

4.2. Sequence of slip activity on positively inclined and negatively inclined slip planes

In Fig. 4(a) only a few slip steps are observed on positively inclined slip planes forming an equilateral triangle after reaching a force of 2 mN during indentation into the {1 1 1} grain. In the load-depth curve, a partial pop-in is visible, which is connected to dislocation nucleation underneath the indenter on positively inclined slip planes. These few dislocations move to the surface and leave behind the surface steps. Because the indentation is stopped at this force, the further dislocation nucleation is prevented. As no surface pile-up is visible, the stress distribution is similar to that of the Hertz solution.

For the other experiments in the {1 1 1} grain, the indentation force is above the pop-in force: pop-ins occur in both cases at around 3.5 mN. Hence, numerous dislocations multiply underneath the indenter and travel on the positively inclined slip planes, leading the significant formation of slip steps on these plane. These

slip events result in the formation of the equilateral triangles as the indentation force increases. After indentation with 5 mN, a few slip steps are observed on negatively inclined glide planes that are located at the equilateral triangle corners. The increased indentation force and deformation introduce a larger imprint, in which slip on positively inclined slip planes dominate. However, slip on negatively inclined planes occurs outside of the imprint, as evident in Fig. 4(b). The domain that is surrounding the imprint and that contains slip steps on the negatively inclined planes grows in size as the deformation increases further, as seen in Fig. 4(c). Finally, the slip step pattern with two triangle sets with point-symmetry is observed.

Due to the crystal orientation, the (1 1 1) and $(1\bar{1}\bar{1})$ planes are almost perpendicular to the surface in the {1 0 1} grain. Hence, the differentiation between positively inclined and negatively inclined planes is more cumbersome. After applying a force of 2 mN, we observed numerous slip steps on both sides of the centerline, which numerically separates between positive and negative inclination angles. Hence, we note slip on the positively and negatively inclined slip planes even at small loads in the imprint and that these slip planes create a parallelogram pattern. In addition, few slip steps are seen on the positively inclined $(11\bar{1})$ and $(1\bar{1}1)$ slip planes in Fig. 6(a). As the indentation force increases to 5 mN, a much higher slip density on the (1 1 1) and $(1\bar{1}\bar{1})$ planes is seen. Moreover, few slip steps form on the negatively inclined $(11\bar{1})$ and $(1\bar{1}1)$ slip planes. These observations of slip steps on $(11\bar{1})$ and $(1\bar{1}1)$ planes also provide the slip-sequence: first on positively inclined and then on negatively inclined planes. This sequence is identical to the sequence seen in the {1 1 1} grain.

It is should be noted that the slip sequence in the {0 0 1} grain is the same as in the {1 1 1} and {1 0 1} grains: first on positively and then on negatively inclined slip planes. In contrast to the {1 1 1} grain, slip occurs on 4 planes in the {0 0 1} grain.

4.3. Numerical model

We execute Finite Element Model simulations to further the understanding of the indentation induced stress distribution and how this stress distribution changes during the development of the indentation pile-up. As evident from the preceding experiments, the order of slip events on positively versus negatively inclined slip planes was independent of the grain orientation, i.e. independent on the crystal anisotropy. Therefore, we calculate the stress state and its dependence on the topology by using a phenomenological isotropic elastic-plastic material model. By purposefully reducing the model complexity, we investigate whether the simplified model is sufficient in explaining the experimental observation: initially slip occurs on positively inclined planes and then slip occurs on negatively inclined planes on the perimeter of the imprint.

We built a 2D model using the Abaqus Explicit framework. We choose the indenter radius and the block size such as to ensure that the contact area is less than 1/6 of the block width. These FEM simulations are scale independent and self-similar: i.e. all deformations scale linearly with the block and radius size. We simulated a rigid indenter with a conical shape (opening angle of 60°) and a radius of 3.7 μm at the tip. The material block has a height and width of 15 μm and 30 μm, respectively, as well as square elements with a size of 0.2 μm. The material is simulated as an elastic-plastic material with an isotropic Young's modulus of 210GPa and a Poison's ratio of 0.3. Plasticity is simulated phenomenologically with linear-isotropic model with a yield stress of 600 MPa and a flow stress of 680 MPa at an equivalent plastic strain of 10%. The indenter – material interaction does not allow for overclosure and uses a minimal friction coefficient of 0.0002 to prevent lateral sliding. To account for the large deformation in the indentation pile-up, we use the explicit model with a time step of 0.1 s, material density of 7.85 kg/m^3 and mass scaling with a time step of 1×10^{-7} s. With these parameters we achieve a numerically efficient simulation and prevent significant elastic waves in the simulation. The indentation speed is chosen as 53 μm/s. The stresses and displacements are exported as text files at an interval of 50 increments.

For the postprocessing, we use model symmetry to average the nodal stresses and displacements, i.e. we improve the accuracy of the dynamic simulation. The principal stresses are evaluated and the maximum shear stress is used as color map. In addition, we determine the resolved shear stress in given orientation and employ an arrow pair to highlight the shear *direction* (positive vs. negative). To investigate the shear *orientation* (0…360) two cases are investigated. In the first case, the orientation of the maximum resolved shear stress is evaluated and plotted in addition to the corresponding maximum shear direction at 90. In the second case, we use two pre-defined slip planes with a Burger's vector of $\langle 1/\sqrt{2}, 1\rangle$ and $\langle -1/\sqrt{2}, 1\rangle$ and the dislocation line direction in the plane of interest. Please note that these Burgers vectors are not perpendicular and – hence – the maximum resolved shear stress is unique. From the Burger's vector and dislocation line, we calculated the plane normal and the resolved shear stress, which is calculate the shear arrows, which are superposed on the maximum shear stress.

In Fig. 9, the maximum resolved shear stress is shown as a colormap. Initially, the stress field is the same as given by the Hertz solution for a sphere interacting with an elastic half-space. The directions of the maximum resolved shear stress are symmetric and occur in directions of positively inclined planes. In this time step, the slip on positively inclined glide planes dominates if specific glide planes are used, as observed in Fig. 9(b). The minor shear stresses in the surrounding are insignificant to initiate plasticity.

After 350 time-steps, the stresses in the contact region have reached the yield strength and the contact domain starts yielding, which produces a pile-up. During this time-step, the directions of the maximum resolved shear stress are forming a shell-like pattern around the indentation axis, see Fig. 9(c). In the inside shell (I), the shear stress is aligned to positively inclined planes. In the middle shell (M), the shear stresses are maximal in the vertical direction, i.e. neither positively nor negatively inclined planes. In the outmost shell (O), the directions of maximum shear stress are diagonal, however the sign of the arrows is inverted compared to the inside shell. It should be noted that shear stresses are elevated in a much larger domain: while significant shear stresses occur only in a small area after 50 time-steps, after 350 time-steps a large area contributes to the shear. The change in shear direction is even more evident in Fig. 9(d), which represents the case if slip occurs on predefined planes. After 350 time-steps, most of the shear on the outside of the contact area has negative inclinations. In addition, dislocations can originate from underneath the indenter and move to the surface. As a result, slip on negative and positive glide planes is predicted in this increment, while the initial snapshot after 50 increments only predicted glide on positive slip planes.

The change compared to the initial snapshot is even more severe after 750 time-steps, i.e. Fig. 9(e) and (f). At this snapshot, a significant pile-up has formed and the shell-like pattern is strengthened. The inside shell (I) has become wider (3 columns of arrows) while the mediate shell (M) with vertical shear has kept its thickness (1 column of arrows). In the distant surrounding, the shear sign inversion has occurred. If only predefined shear directions are analyzed, the cone shape representing negative inclined slip planes has gained dominance. In the domain of shear on negatively inclined planes, these resolved shear stresses far exceed the shear stresses in the Hertzian contact domain after 50 time-steps. This finding shows that if plasticity has originated from underneath the indenter in the initial deformation, the stresses in the outside

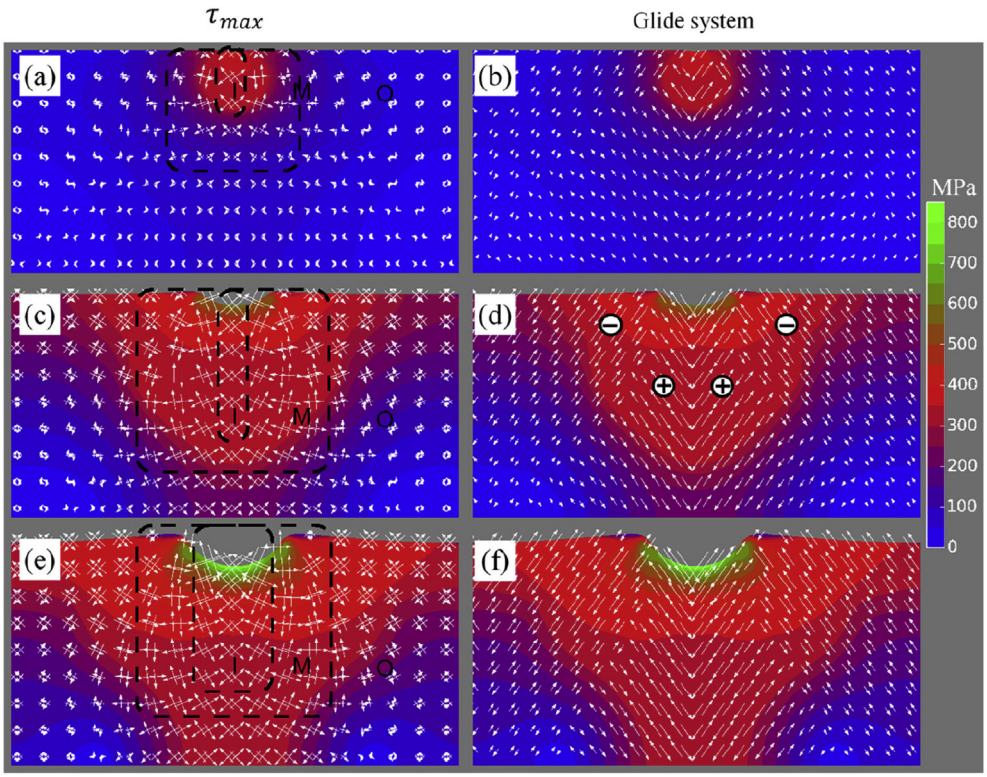

Fig. 9. Maximum shear stress, i.e. principal shear stress in MPa, distribution after (a) & (b): 50, (c) & (d): 350 and (e) & (f): 750 time-steps. (a), (c) and (e): superimposed arrow pair showing the direction of maximum shear stresses with one degree resolution. (b), (d) and (f): superimposed arrow pair showing the maximum of two shear directions, representing a FCC crystal in 2D. The arrow length shows the magnitude of the resolved shear stress. In (a), (c) and (e): the black dashed lines mark the inside (I), middle (M) and outside (O) shell, that is used in the text.

domain are now so high as to lead to slip on negatively inclined slip planes.

As such, the isotropic elastic-plastic simulations support the sequence of slip plane activation. Initially, plasticity occurs on positively inclined planes due to the stress distribution that is given by the Hertz solution, i.e. for a sphere and a flat surface. As the indentation continues the stress state changes, i.e. it does not remain self-similar. The evolving surface topology of the pile-up results in an outer shell of sufficiently high stresses that lead to slip on negatively inclined planes.

Hence, the simplified model is sufficient in explaining the observed sequence of slip on differently inclined planes that were observed in the grains of {1 1 1}, {1 0 1} and {0 0 1} orientation. It should be noted that in orientations with less symmetry the experimental results differ and that the simplified model is not applicable if no symmetry axis exists. Further studies might help to investigate whether these findings are generally applicable.

5. Conclusions

Based on the systematic identification of slip plane activation during nanoindentation and based on the study of the inclination of the activated planes for three grains with varying loads, the following conclusions are drawn:

- Slip steps on positively inclined slip planes are activated in the early stage of the indentation. This slip activity corresponds to the stress distribution according to the Hertz solution. As a result of this plasticity, dislocation pile-ups form.
- After pile-up formation, the contact is not captured by the Hertz solution as it does not account for the evolution of the pile-up, i.e. surface topography. This change in stress state results in a change of activated slip planes: slip on negatively inclined slip planes. While slip on positively inclined planes occurred in the contact zone of the indenter, the surrounding of the imprint is dominated by slip on negatively inclined slip planes.
- The inclination of the slip planes (i.e. positively inclined or negatively inclined) is identified either (1) through EBSD, (2) coupling EBSD-ECCI or (3) coupling EBSD-AFM. The coupling of EBSD and ECCI provided the most reliable identification for general grain orientations.
- In the austenitic steel, the slip steps are mainly a consequence of conventional dislocation loops (rather than prismatic dislocation loops) travelling on positively and negatively inclined slip planes to the free surface.

CRediT authorship contribution statement

Wenzhen Xia: Conceptualization, Methodology, Data curation, Formal analysis, Writing - original draft. **Gerhard Dehm:** Supervision, Writing - review & editing. **Steffen Brinckmann:** Conceptualization, Software, Funding acquisition, Supervision, Writing - review & editing.

Acknowledgements

The authors appreciate the funding of the Deutsche Forschungsgemeinschaft DFG within project BR-3947/5-1.

Appendix A. Supplementary data

Supplementary data to this article can be found online at https://doi.org/10.1016/j.matdes.2019.108169.

References

[1] D. Hull, D.J. Bacon, Introduction to Dislocations, Elsevier, 2011.
[2] G. Gottstein, Physical Foundations of Materials Science, Springer Science & Business Media, 2013.
[3] C.A. Schuh, Nanoindentation studies of materials, Mater. Today 9 (5) (2006) 32–40.
[4] W.C. Oliver, G.M. Pharr, An improved technique for determining hardness and elastic-modulus using load and displacement sensing indentation experiments, J. Mater. Res. 7 (6) (1992) 1564–1583.
[5] W.C. Oliver, G.M. Pharr, Measurement of hardness and elastic modulus by instrumented indentation: advances in understanding and refinements to methodology, J. Mater. Res. 19 (1) (2004) 3–20.
[6] S.W. Chen, Y. Miyahara, A. Nomoto, Crystallographic orientation dependence of nanoindentation hardness in austenitic phase of stainless steel, Philos. Mag. Lett. 98 (11) (2018) 473–485.
[7] S. Higashino, M. Miyake, A. Takahashi, Y. Matamura, H. Fujii, R. Kasada, T. Hirato, Evaluation of the hardness and Young's modulus of electrodeposited Al-W alloy films by nano-indentation, Surf. Coat. Technol. 325 (2017) 346–351.
[8] W.D. Nix, H.J. Gao, Indentation size effects in crystalline materials: a law for strain gradient plasticity, J. Mech. Phys. Solids 46 (3) (1998) 411–425.
[9] H. Song, H. Yavas, E. Van der Giessen, S. Papanikolaou, Discrete dislocation dynamics simulations of nanoindentation with pre-stress: hardness and statistics of abrupt plastic events, J. Mech. Phys. Solids 123 (2019) 332–347.
[10] V. Maier-Kiener, B. Schuh, E.P. George, H. Clemens, A. Hohenwarter, Insights into the deformation behavior of the CrMnFeCoNi high-entropy alloy revealed by elevated temperature nanoindentation, J. Mater. Res. 32 (14) (2017) 2658–2667.
[11] T.Y. Chen, L.Z. Tan, Z.Z. Lu, H.X. Xu, The effect of grain orientation on nanoindentation behavior of model austenitic alloy Fe-20Cr-25Ni, Acta Mater. 138 (2017) 83–91.
[12] A. Leitner, V. Maier-Kiener, D. Kiener, Dynamic nanoindentation testing: is there an influence on a material's hardness? Mater. Res. Lett. 5 (7) (2017) 486–493.
[13] R.S. Ganji, P.S. Karthik, K.B.S. Rao, K.V. Rajulapati, Strengthening mechanisms in equiatomic ultrafine grained AlCoCrCuFeNi high-entropy alloy studied by micro- and nanoindentation methods, Acta Mater. 125 (2017) 58–68.
[14] V. Maier-Kiener, K. Durst, Advanced nanoindentation testing for studying strain-rate sensitivity and activation volume, Jom-Us 69 (11) (2017) 2246–2255.
[15] M. Liu, A.K. Tieu, C.T. Peng, K. Zhou, Explore the anisotropic indentation pile-up patterns of single-crystal coppers by crystal plasticity finite element modelling, Mater. Lett. 161 (2015) 227–230.
[16] M. Liu, C. Lu, A.K. Tieu, Crystal plasticity finite element method modelling of indentation size effect, Int. J. Solids Struct. 54 (2015) 42–49.
[17] M.A. Lodes, A. Hartmaier, M. Goken, K. Durst, Influence of dislocation density on the pop-in behavior and indentation size effect in CaF2 single crystals: experiments and molecular dynamics simulations, Acta Mater. 59 (11) (2011) 4264–4273.
[18] A. Montagne, V. Audurier, C. Tromas, Influence of pre-existing dislocations on the pop-in phenomenon during nanoindentation in MgO, Acta Mater. 61 (13) (2013) 4778–4786.
[19] C. Tromas, Y. Gaillard, J. Woirgard, Nucleation of dislocations during nanoindentation in MgO, Philos. Mag. 86 (33–35) (2006) 5595–5606.
[20] C. Tromas, J.C. Girard, V. Audurier, J. Woirgard, Study of the low stress plasticity in single-crystal MgO by nanoindentation and atomic force microscopy, J. Mater. Sci. 34 (21) (1999) 5337–5342.
[21] M. Vellednitskaya, V. Rozhanskii, L. Comolova, G. Saparin, J. Schreiber, O. Brümmer, Investigation of the deformation mechanism of MgO crystals affected by concentrated load, Phys. Status Solidi A 32 (1) (1975) 123–132.
[22] K.A. Nibur, D.F. Bahr, Identifying slip systems around indentations in FCC metals, Scr. Mater. 49 (11) (2003) 1055–1060.
[23] K.A. Nibur, F. Akasheh, D.F. Bahr, Analysis of dislocation mechanisms around indentations through slip step observations, J. Mater. Sci. 42 (3) (2007) 889–900.
[24] B. Eidel, Crystal plasticity finite-element analysis versus experimental results of pyramidal indentation into (001) fcc single crystal, Acta Mater. 59 (4) (2011) 1761–1771.
[25] Y. Wang, D. Raabe, C. Kluber, F. Roters, Orientation dependence of nanoindentation pile-up patterns and of nanoindentation microtextures in copper single crystals, Acta Mater. 52 (8) (2004) 2229–2238.
[26] Z.F. Wang, J.J. Zhang, H. ul Hassan, J.G. Zhang, Y.D. Yan, A. Hartmaier, T. Sun, Coupled effect of crystallographic orientation and indenter geometry on nanoindentation of single crystalline copper, Int. J. Mech. Sci. 148 (2018) 531–539.
[27] C.S. Han, A. Hartmaier, H.J. Gao, Y.G. Huang, Discrete dislocation dynamics simulations of surface induced size effects in plasticity, Mat Sci Eng a-Struct 415 (1–2) (2006) 225–233.
[28] A. Widjaja, E. Van der Giessen, A. Needleman, Discrete dislocation modelling of submicron indentation, Mat Sci Eng a-Struct 400 (2005) 456–459.
[29] M.C. Fivel, C.F. Robertson, G.R. Canova, L. Boulanger, Three-dimensional modeling of indent-induced plastic zone at a mesoscale, Acta Mater. 46 (17) (1998) 6183–6194.
[30] M. Verdier, M. Fivel, I. Groma, Mesoscopic scale simulation of dislocation dynamics in fcc metals: principles and applications, Model Simul Mater Sc 6 (6) (1998) 755–770.
[31] J. Gagel, D. Weygand, P. Gumbsch, Formation of extended prismatic dislocation structures under indentation, Acta Mater. 111 (2016) 399–406.
[32] Y. Miura, Punched-out dislocation rosettes in low-dislocation-density copper, J. Appl. Phys. 43 (6) (1972) 2917–2918.
[33] Y. Miura, H. Nakamura, H. Kaieda, Prismatic dislocation loops in copper revealed by X-ray topography, J. Jpn. Inst. Metals 17 (12) (1976) 793–798.
[34] C. Begau, J. Hua, A. Hartmaier, A novel approach to study dislocation density tensors and lattice rotation patterns in atomistic simulations, J. Mech. Phys. Solids 60 (4) (2012) 711–722.
[35] C. Begau, A. Hartmaier, E.P. George, G.M. Pharr, Atomistic processes of dislocation generation and plastic deformation during nanoindentation, Acta Mater. 59 (3) (2011) 934–942.
[36] A. Stukowski, A. Arsenlis, On the elastic-plastic decomposition of crystal deformation at the atomic scale, Model Simul Mater Sc 20 (3) (2012).
[37] S.S. Jiao, W.J. Tu, P.G. Zhang, W. Zhang, L.G. Qin, Z.M. Sun, J. Chen, Atomistic insights into the prismatic dislocation loop on Al (100) during nanoindentation investigated by molecular dynamics, Comput. Mater. Sci. 143 (2018) 384–390.
[38] I.A. Alhafez, C.J. Ruestes, E.M. Bringa, H.M. Urbassek, Nanoindentation into a high-entropy alloy—an atomistic study, J. Alloys Compd. 803 (2019) 618–624.
[39] J. Varillas, J. Ocenasek, J. Torner, J. Alcala, Unraveling deformation mechanisms around FCC and BCC nanocontacts through slip trace and pileup topography analyses, Acta Mater. 125 (2017) 431–441.
[40] R.E. Schramm, R.P. Reed, Stacking fault energies of seven commercial austenitic stainless steels, Metall. Trans. A. 6 (7) (1975) 1345.
[41] S. Zaefferer, N.N. Elhami, Theory and application of electron channelling contrast imaging under controlled diffraction conditions, Acta Mater. 75 (2014) 20–50.
[42] Y. Xiong, T.T. He, H.P. Li, Y. Lu, F.Z. Ren, A.A. Volinsky, Annealing effects on microstructure and mechanical properties of cryorolled Fe-25Cr-20Ni steel, Mat Sci Eng a-Struct 703 (2017) 68–75.
[43] Y. Miura, F. Higuchi, H. Era, Dislocation multiplication sources in copper revealed by X-ray topography, Philos. Mag. A 71 (6) (1995) 1363–1373.
[44] H.J. Chang, M. Fivel, D. Rodney, M. Verdier, Multiscale modelling of indentation in FCC metals: from atomic to continuum, Cr Phys 11 (3–4) (2010) 285–292.
[45] G.Z. Voyiadjis, M. Yaghoobi, Large scale atomistic simulation of size effects during nanoindentation: dislocation length and hardness, Mat Sci Eng a-Struct 634 (2015) 20–31.